CMS CFT 09-011

DRAFT
CMS CRAFT Performance Note

The content of this note is intended for CMS internal use and distribution only

2009/09/03
Archive Id: 1.2
Archive Date: 2009/09/03 18:53:09

Performance of the CMS Cathode Strip Chambers with Cosmic Rays

The CSC DPG
CERN

Abstract

The Cathode Strip Chambers (CSCs) constitute the primary muon tracking device in the CMS endcaps. Their performance has been evaluated using data taken during a long cosmic ray run in Fall 2008. Distributions of basic global quantities are well reproduced by the simulation. Noise levels are low according to measurement, and nearly all anode and cathode channels deliver data. Efficiencies have been measured and are very high, and the spatial resolution of the chambers has been studied and measured, with good results. Finally, a brief exploratory study of the potential timing capabilities of the CSCs has been completed.

1 Introduction

The Cathode Strip Chambers (CSCs) comprise an essential component of the CMS muon detector, providing precise tracking and triggering of muons in the endcaps. Their performance is critical to many planned physics analyses based on muons. An early assessment of their performance is possible using data recorded during the Fall of 2008 as part of the *Cosmic Run At Four Tesla* (CRAFT) campaign. This paper summarizes the early results obtained from the analysis of those data.

The CRAFT campaign involved all installed subdetector systems, most of which were nearly fully operational, as described in other reports included in this volume. Close to 300 M cosmic ray muon triggers were recorded while the magnet was at full field (3.8 T). Of these, roughly a fifth originated from the CSCs.

The CSC subdetector is composed of rings of trapezoidal chambers mounted on eight disks - four in each endcap. The rings of chambers are designated by ME$\pm S/R$, where the $\pm$ sign indicates the endcap, S indicates the disk (or "station"), and R is the ring number. A drawing of CMS highlighting the CSC subdetector is shown in Fig. 1. Each chamber contains six detecting layers each composed of an anode wire plane between two planar copper cathodes, one continuous, the other segmented in strips to provide coordinate readout [1]. The CSCs measure the ϕ coordinates of muon tracks well, as the bending of the muon trajectories in the magnetic field returned through the iron disks is mainly about the $\hat{s}$ direction, where $\hat{s}$ is a unit vector in cylindrical coordinates pointing away from the beam line. The strips describe constant ϕ values, and hence are trapezoidal in shape, like the chambers themselves. A high precision is achieved on the basis of the shape of the charge distribution on three consecutive strips; this allows an adequate measurement of the muon momentum as needed for triggering purposes. The anode wires provide a relatively approximate measure of the radial coordinate.

The readout of a CSC is triggered by the presence of Anode and Cathode Local Charged Track patterns, referred to as ALCT and CLCT, respectively. They are defined in the trigger logic [2, 3]. A correlated LCT is also defined and used in triggering the readout of the chamber. The final CSC muon trigger is generated by the CSC track finder and sent to the general muon trigger processor. For CRAFT, events were recorded with a very loose CSC trigger based on the logical "OR" of the trigger signals of all individual chambers. The rate of this loose trigger was about 60 Hz. The drift tube barrel muon detector also provided cosmic muon triggers at about four times this rate.

In the sections that follow, we present a selection of distributions characterizing the useful cosmic ray flux through the endcaps, an assessment of the CSC anode electronics, results on the measurement of efficiency and resolution, and some basic information about the timing capabilities of the CSCs. Most of these results are documented more fully in Ref. [4–7]. We begin with a brief account of the commissioning of the system and of the basics of offline reconstruction.

2 Commissioning the CSCs

The assembly of the CSCs included a comprehensive commissioning regimen to verify chamber performance during production [8]. This set of tests was performed again on each chamber upon arrival at CERN, and multiple times following installation on the endcap disks on the surface during 2005-7. In 2007, the disks were lowered into the CMS cavern at Point 5, and the full set of services and infrastructure became available early in 2008. At this time, a team

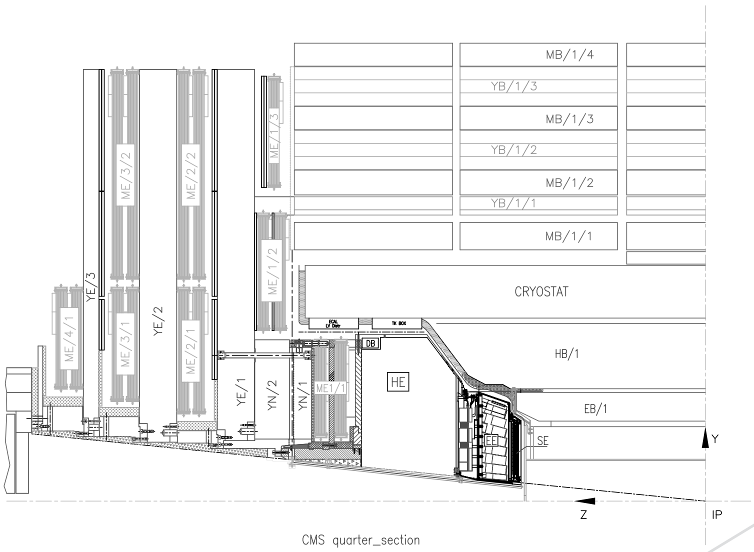

Figure 1: A cross-sectional view of the CMS detector, highlighting the CSCs.

of physicists and engineers expanded the scope of the commissioning program from checking one chamber at a time to covering the entire set of 468 chambers as a subdetector system.

The commissioning effort included the following tasks: establishing inter-component communication, loading new versions of firmware to the electronics boards, turning on and configuring all components in a robust way, and measuring the parameters necessary to ensure synchronization of the system. An essential aspect of the commissioning effort was to diagnose what components, including cables, had problems so that they could be fixed before the CMS detector was closed. In addition, the development of a suite of software tools was essential to bring the CSC system online - a system whose size requires procedures and rigor akin to an assembly line. By the time of CRAFT, more than 96% of the readout channels were live. Fig 2 shows that hits could be reconstructed successfully in most of the chambers.

During CRAFT, the CSCs functioned well over a period of several weeks, and they were included in the readout for about 80% of the CRAFT running period. The system was exposed to a different set of issues which had not been encountered during the normal commissioning period.

3 Local Muon Reconstruction

Raw data recorded from the detector are unpacked into integer-based objects called “digis.” There are digi collections for the strip signals, the wire signals, and the local charged trigger tracks (LCTs). The information stored in the digis is processed to produce a collection of objects called “rechits” with measured x and y coordinates at a known z coordinate. These represent the measurement of the intersection point between the track and a CSC layer. The rechits reconstructed in a given chamber are used to form a straight-line segment, which is fit to provide a measure of the muon trajectory in the chamber. Only one rechit is used from any given layer,

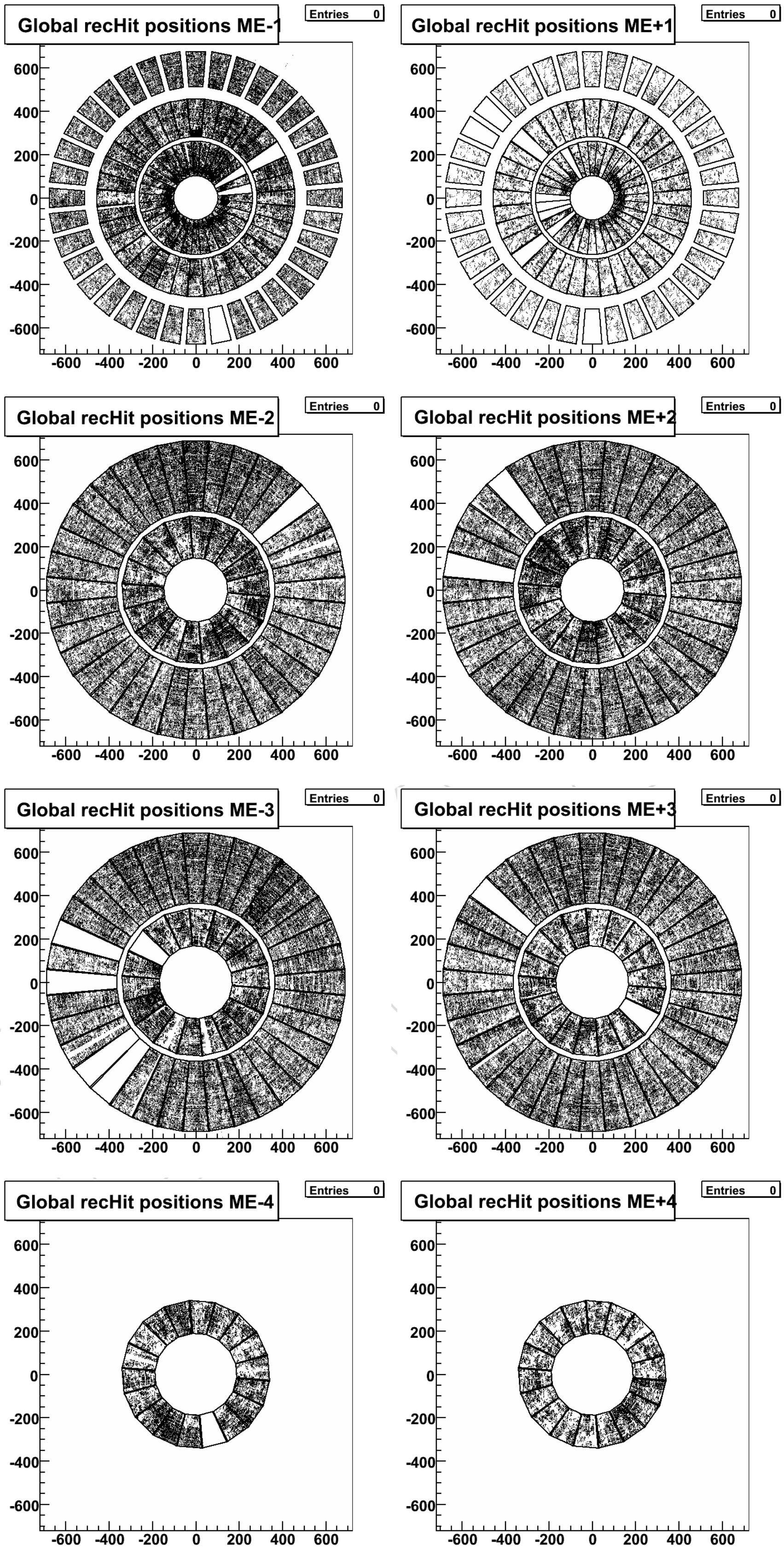

Figure 2: Distributions of rechits reconstructed from a portion of the CRAFT data. Nearly all of the chambers were fully operational. The less than 3% of chambers that did not provide data have been repaired since CRAFT.

and a minimum number of three rechits is required. The majority of segments have six rechits, while a modest fraction have fewer due to the impact of δ-ray electrons and the boundaries of the chamber. These segments are used to seed the reconstruction of muon tracks based on muon chamber data only – these are called “stand-alone muons” [9]. Due to the very broad range of cosmic ray incident angles, only a small fraction of the stand-alone muons can be matched to reconstructed tracks in the Silicon tracker, especially those in the endcaps.

The alignment of the muon chambers and of the Si tracker is based on two complementary methods - the first uses lasers and specially placed sensors, while the other uses muon tracks. The first method provided basic information about the position of the endcap disks relative to the barrel, and this information was used in the reconstruction of the CRAFT data. Alignment of the muon endcap detectors with tracks is ongoing. For more details, see Ref. [10] in this volume.

The magnetic field map was verified by examining the deflection of selected muon tracks passing through the disks and the Si tracker. It was shown to be accurate to 5% or better [11].

Simulated data sets were produced using the `CMSCGEN` Monte Carlo event generator, which is configured to reproduce the CRAFT data as closely as possible [12]. The simulated data, the reconstructed CRAFT data, and the results presented in this paper are based on official CMS reconstruction code releases dating from the Spring of 2009.

4 Basic Information from Cosmic Rays

Most cosmic rays above ground have an energy of at most a few GeV [13]. In the underground cavern at Point 5, the energy spectrum is shifted to somewhat higher values. Muons must have energies of at least a few GeV in order to pass through three consecutive CSC stations, since the iron disks between them are approximately 34 X_0 thick. Most reconstructed cosmic ray muons have only a few GeV, so multiple scattering in the iron yokes can displace the muon’s trajectory by several centimeters with respect to the ideal trajectory.

Most of the muons triggered in the endcaps are not useful because their trajectories are steeply inclined or pass through only an edge of one of the endcaps. Only a minute fraction of the recorded cosmic ray muons follow a useful path through the endcaps, and satisfy the nominal geometric requirements for the efficient triggering and readout of the CSCs, as explained in detail below.

In order to secure a sample of useful events, a skim of the primary data set selected events in which at least three chambers had hits, and in which at least two segments had been reconstructed. Events with very many rechits or segments were excluded, since they were likely contain muon-induced showers which would frustrate these performance studies. These relatively loose criteria reduced the data sample with CSC triggers by a factor of twenty, and enabled direct comparisons of the simulated data to the real CRAFT data.

Distributions of simple quantities such as the total number of rechits per event and the number of segments per event are shown in Fig. 3. The requirement of three chambers with hits suppresses entries at the low end of these distributions.

Further information about the reconstructed segments is shown in Fig. 4. The first plot shows the number of hits on a segment, which must be at least three and cannot be more than six. Most segments have one rechit in every layer, and this is well reproduced by the simulation. The second and third plots show the inclinations of the segments, namely, the polar angle

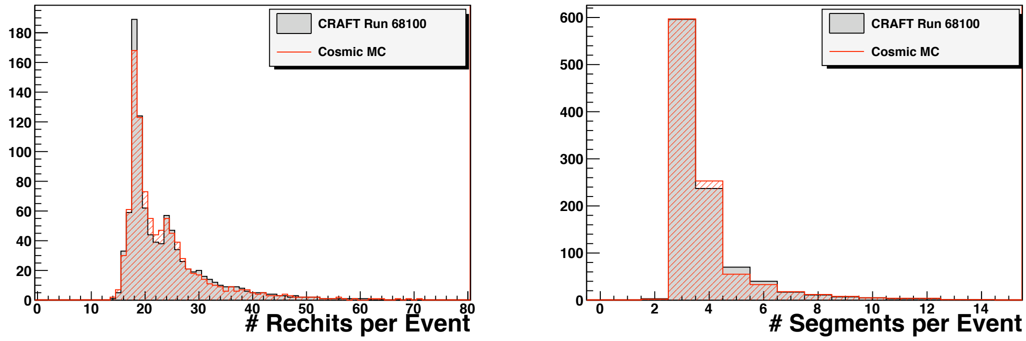

Figure 3: A comparison of the simulated events to the real CRAFT events for simple global quantities. *LEFT:* total number of rechits per event. *RIGHT:* total number of segments per event.

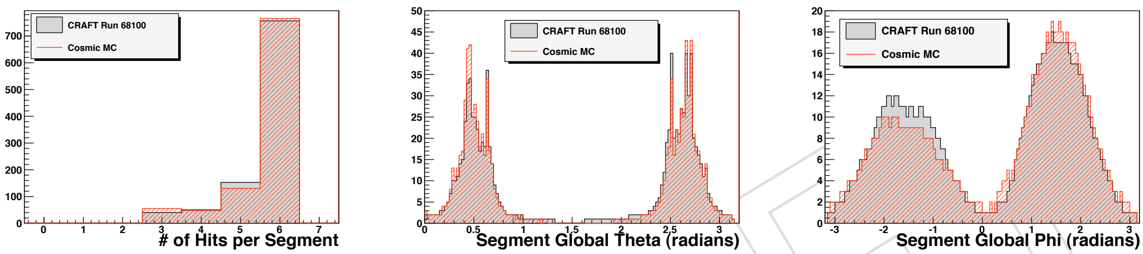

Figure 4: A comparison of the simulated events to the real CRAFT events for reconstructed segment quantities. *LEFT:* number of hits per segment. *MIDDLE:* global polar angle. The two endcaps are clearly visible (ME+ at $\theta \sim 0.5$ and ME- at $\theta \sim 2.7$). *RIGHT:* global azimuthal angle. The bump at $\phi \sim 1.8$ corresponds to the upward vertical direction, and $\phi \sim -1.8$, to the downward.

("global theta") and the azimuthal angle ("global phi"). The vertical nature of the cosmic ray flux is evident in these distributions, which are very well reproduced by the simulation.

Finally, basic distributions for stand-alone muons in the endcaps are presented in Fig. 5. The first plot shows the distribution of the number of CSC rechits on the track. The distribution of simulated events differs from the CRAFT distribution in part because the alignment of the muon endcaps has not been completed. The second plot shows the distribution of polar angles computed at the point on the stand-alone muon track closest to the center of the detector. The agreement is very good.

5 Noise

An assessment of the fraction of nonfunctional and noisy channels must be made before any discussion of efficiencies or resolution. Setting aside the few chambers that were turned off due to problems with high voltage, low voltage, or a very small number of malfunctioning electronics boards, the number of anode wire and cathode strip channels that failed to give data were below 1% of the total. Given the six-layer redundancy of each chamber, and the redundancy of the four disks in each endcap, the impact of these very few dead channels was negligible.

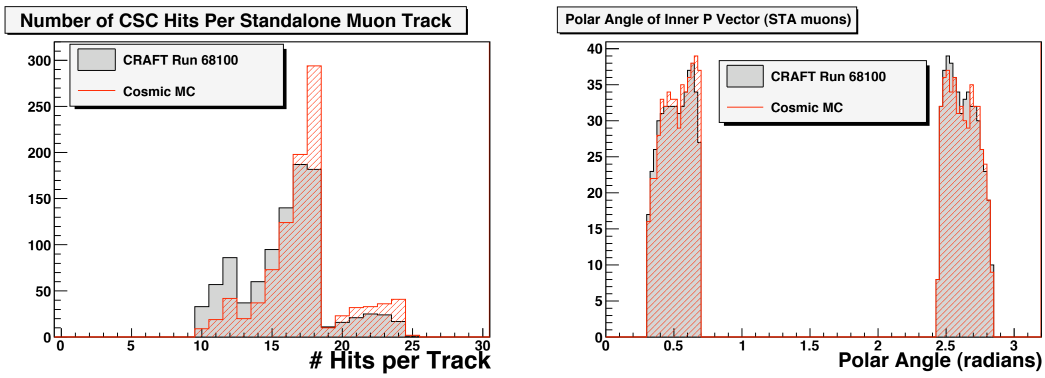

Figure 5: A comparison of the simulated events to the real CRAFT events for stand-alone muon tracks. *LEFT:* number of hits per track. *RIGHT:* global polar angle.

Noise can have two different deleterious effects, in principle: it can generate extra hits which interfere with the reconstruction of muon tracks, and it can smear or distort the measurement of the charge registered on the strips, thereby smearing or distorting the calculated strip coordinates. We have used the CRAFT data to make a basic assessment of the noise on both the anode wire and cathode strip channels.

The first two 50 ns time bins in a strip signal are reserved for an estimate of the *base line* and should be free of signal. Prior to the beginning of CRAFT, the overall timing of the CSCs was adjusted to ensure that this was the case. Consequently, the difference in the ADC values recorded for the first two time bins, $Q_1 - Q_0$, should be zero, aside from any random fluctuations due to electronics noise [1]. In order to be very sure that no signal contributed to Q_1 and Q_0, strip channels with a sum of charges 13 ADC counts or more above base line were omitted.

The rms of the distribution of $\Delta_{01} \equiv Q_1 - Q_0$, σ_{01}, is taken to be a measure of noise, and was obtained for all sets of 16 strip channels handled by the cathode front-end boards, for all chambers. Fig. 6 shows the distribution of all σ_{01} values.

The typical values are about 3 ADC counts or slightly larger; there is little spread indicating excellent uniformity. There are absolutely no large values, indicating no oscillating or otherwise noisy channels at all.

Two peaks can be discerned in Fig. 6, corresponding to smaller and larger chambers. Fig. 7 displays some example distributions for Δ_{01} showing that the rms is larger for the larger chambers (ME$\pm$2/2 in the figure). The distributions are Gaussian with no tails or asymmetry.

The anode wire signals normally extend over one or two 25 ns time bins. A noisy channel, however, will rise above threshold in more time bins, so a useful quantity with which to identify noisy channels is the number of time bins for which a given anode hit is *on*, denoted here by N_{on}. The distribution of N_{on} for all anode channels in a particular chamber is shown in Fig. 8, on a semi-log plot. A very small tail for $N_{\text{on}} > 2$ can be seen. The number of noisy anode wire channels is estimated to be less than 0.1%.

[1] Slow components in the noise on a channel will not be efficiently detected this way.

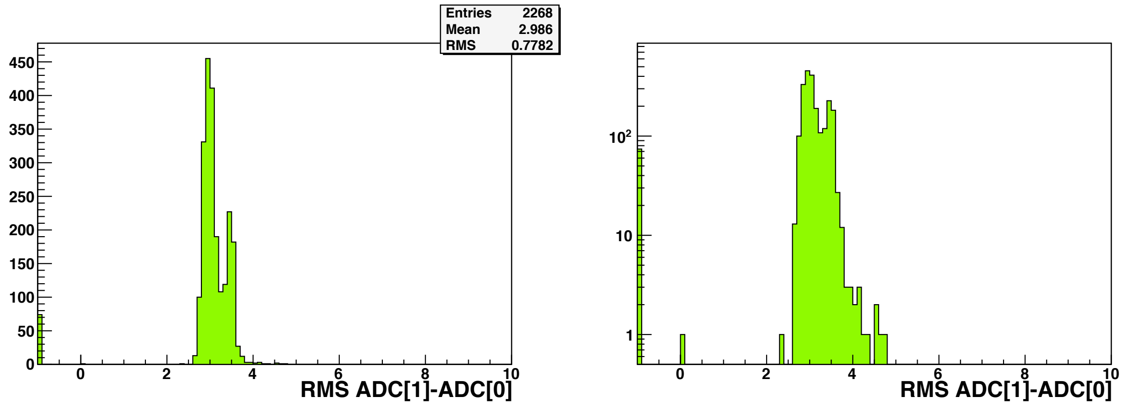

Figure 6: Distribution of all σ_{01} values, i.e., the rms of the difference in the first two ADC readings, on a linear scale (left) and a log scale (right)

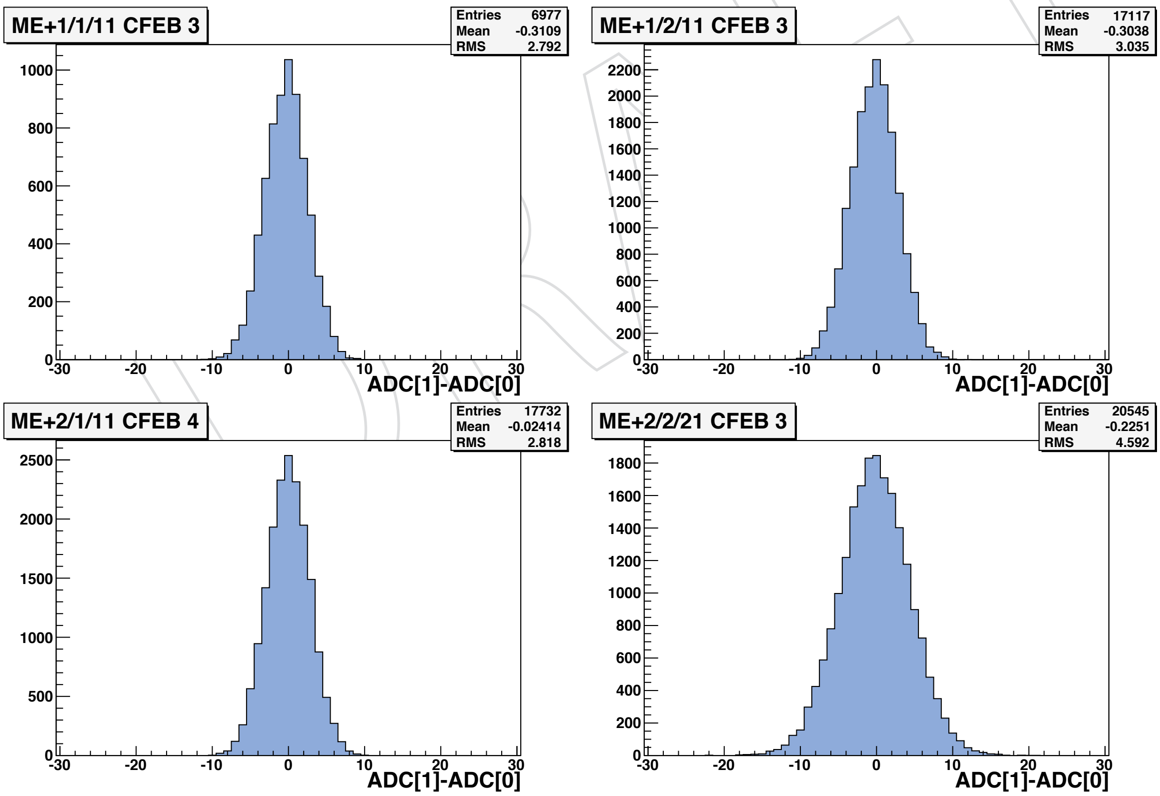

Figure 7: Four examples of Δ_{01} distributions, where Δ_{01} is the difference in the first two ADC readings for a strip.

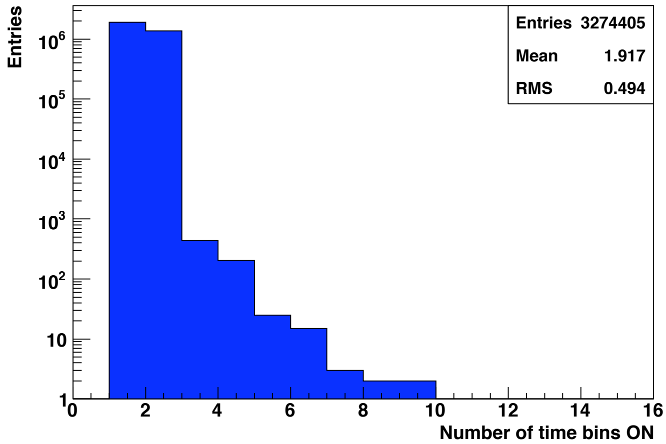

Figure 8: A semi-log plot of N_{on} (the number of time bins for which there is signal) for all anode wire channels in ME-2/1/9

6 Efficiency

The goal of this study is to measure the absolute efficiency of each step in the reconstruction of muons in the CSCs, from the generation of ALCTs and CLCTs through to segment reconstruction. By design, for good muons coming from the interaction point, all steps should be highly efficient. The method described here uses two chambers to "tag" a muon that passes through a designated "probe" chamber. When computing the efficiency of each step, the same tagged sample (i.e., the "denominator" in the efficiency calculation) is used for all steps.

For efficiency measurements, we need a well-defined muon track which is independent of the measurements in the chamber under investigation. We use muon tracks reconstructed in several CSCs without any information from the Si tracker – these are the "stand-alone" muons. The number of useful stand-alone muons is adequate for the present purposes, thanks to the redundancy of the muon endcap system. To minimize the impact of possible difficulties coming from multiple scattering, energy loss, and tracking in a strong magnetic field, a chamber is probed only if it lies between the endpoints of the track. Consequently, at least two independent measurements of the muon track are needed, and only interpolation and not extrapolation to the probe chamber is used. Some rings, namely ME$\pm$1/1, ME$\pm$4/1 and ME$-$3/2 cannot be covered by this study, although hits in the Resistive Plate Chambers (RPCs) allow coverage of ME+3/2.

A typical event selected for these efficiency measurements contains three or four CSCs contributing to a good stand-alone muon track. Since the trigger efficiency is generally high (see below), and a trigger from any one of these chambers sufficed to produce a trigger for read out of CMS, we assume that any trigger bias in the results is negligible.

We place cuts on the predicted position of the muon in the probe chamber to avoid losses due to insensitive regions at the periphery of the chamber and at the boundaries of the high voltage segments. Fig. 9 shows distributions of the difference between the measured position of a segment in the probe chamber and the predicted position, obtained by propagating the muon track from another station to the probe chamber, taking the magnetic field, multiple scattering and energy loss into account. In this figure, the local coordinate X runs parallel to the wires, and is measured primarily by the strips, while Y runs perpendicular to the wires, and is measured

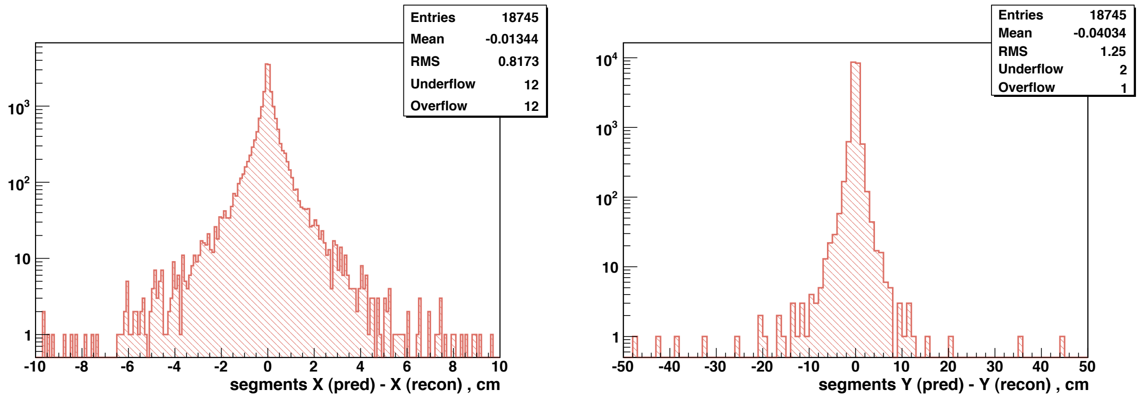

Figure 9: Differences between the predicted positions of a segment and the position of the reconstructed segment in the probe chamber. ΔX is on the left, and ΔY is on the right, where X and Y are local coordinates. X is measured primarily by the strips, and Y, by the wires

by the wire signals. According to these distributions, nearly all of the tracks fall within 10 cm of the predicted position.

A set of stringent criteria is used to select "good" tracks for the denominator of all efficiency calculations [5]. Only one stand-alone muon track is allowed in an endcap. This track has to have at least a minimum number of hits, and to be reconstructed well, as indicated by the χ^2 and the relative error on the momentum. The momentum itself should be in a reasonable range, $25 < p < 100$ GeV/c. A track satisfying these requirements is propagated to a designated ring of CSC chambers to ascertain which chamber is the probe chamber. If the interpolated point lies within 10 cm of the edges of the chamber or dead regions defined by high voltage segment boundaries, then the chamber is skipped. The tracks which pass all of these criteria are the "probe" tracks.

6.1 Results from CRAFT

The following sections report the details of the measurements and the values of the efficiency for each step in the CSC local reconstruction.

6.1.1 LCT Efficiencies

The ALCT and CLCT efficiencies are measured independently. For a given chamber, the ALCT and CLCT digis are unpacked to test for the presence of a valid ALCT or CLCT. If they are present anywhere in the chamber, then the trial is a "success" and the chamber is "efficient" for that event.

The ALCT wire patterns and the CLCT strip patterns were designed to be efficient only for muons originating from the interaction point [3]. The wire group width varies between 1.5 and 5 cm for different chambers. The distance between layers is 2.54 cm, except for the ME1/1 chambers, for which it is 2.2 cm. The range of track inclination (dy/dz in local coordinates) which should give efficient ALCT response is $-0.69 < dy/dz < 0$ for smaller chambers, and $-1.97 < dy/dz < 0$ for larger chambers. Similarly, for the CLCT response the range is $|dx/dz| < 0.24$ for smaller, and 0.63 for larger chambers. For collision data, the muons will naturally have inclination angles within these ranges. Muons from cosmic rays, however, arrive at a wide variety of angles. To suppress the muons which are not likely to fire the ALCT and/or CLCT triggers, we apply cuts on the slopes of the muon tracks interpolated through

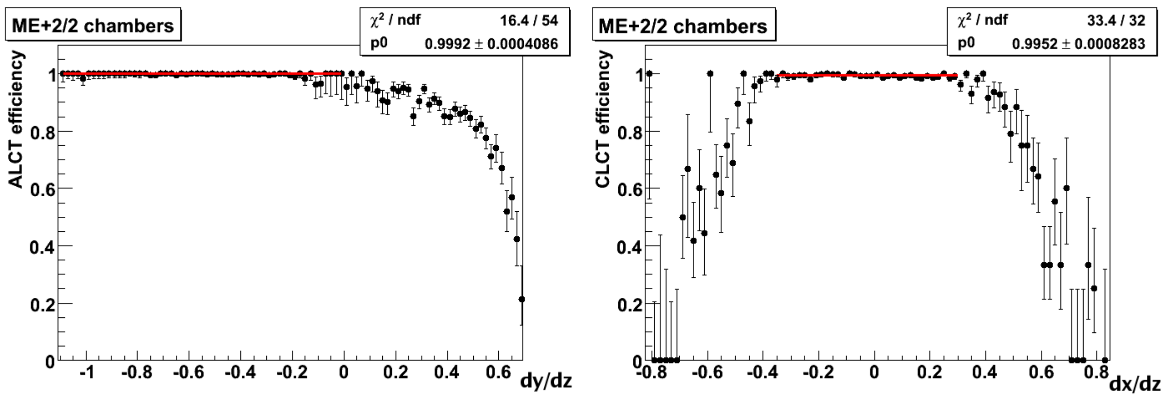

Figure 10: LEFT: ALCT efficiency as a function of the track inclination, dy/dz in local coordinates. RIGHT: CLCT efficiency as a function of the track inclination, dx/dz in local coordinates

the chamber:

$$-0.8 < \frac{dy}{dz} < -0.1 \qquad \text{and} \qquad \left|\frac{dx}{dz}\right| < 0.2. \tag{1}$$

One could adjust these ranges for the various rings of chambers, but the impact on the efficiency measurements is negligible. All the efficiencies measured with CRAFT data include these requirements in the event selection.

The variation of the ALCT efficiency as a function of dy/dz is shown in Fig. 10 (left). For this figure, the cut on dy/dz was not applied, although the cut on dx/dz was applied. Similarly, the variation of the CLCT efficiency as a function of dx/dz is shown in Fig. 10 (right), with the cut on dx/dz relaxed, and the cut on dy/dz applied. The results shown in these plots are based on data from chambers 5–13 in ring ME+2/2 which were known to be operating well. In both figures, clear plateaus can be seen which were fit with level functions to ascertain the efficiency. Very high values in excess of 0.999 are observed, confirming earlier results obtained with cosmic rays [18].

6.1.2 Strip and Wire Group Efficiencies

In principle, the presence of an ALCT and CLCT should trigger the readout of the chamber, and hence, signals on the wires and strips should be present in the raw data, or equivalently, in the strip and wire digis. The efficiency for strip and wire digis are measured independently. The probe is given by a good track passing through the given chamber.

The efficiencies of strips, wire groups and rechits are defined naturally per layer. If the layer measurements are independent, then the average efficiency per chamber would be

$$\bar{\epsilon} = \frac{\sum_i \epsilon_i}{L} = \frac{\sum_i n_i}{N \times L} \tag{2}$$

with an estimated uncertainty of

$$\Delta\bar{\epsilon} = \sqrt{\frac{\bar{\epsilon} \times (1 - \bar{\epsilon})}{L \times N}}, \tag{3}$$

where $L = 6$ is the number of layers, ϵ_i is the efficiency in layer i ($i = 1, .., 6$), n_i is the number of efficient cases ("successes") for layer i, and N is the number of probe tracks. In principle, there might be events with a simultaneous loss of information from all six layers, in which case Eq. 3 is incorrect. There is no evidence for any such correlated losses.

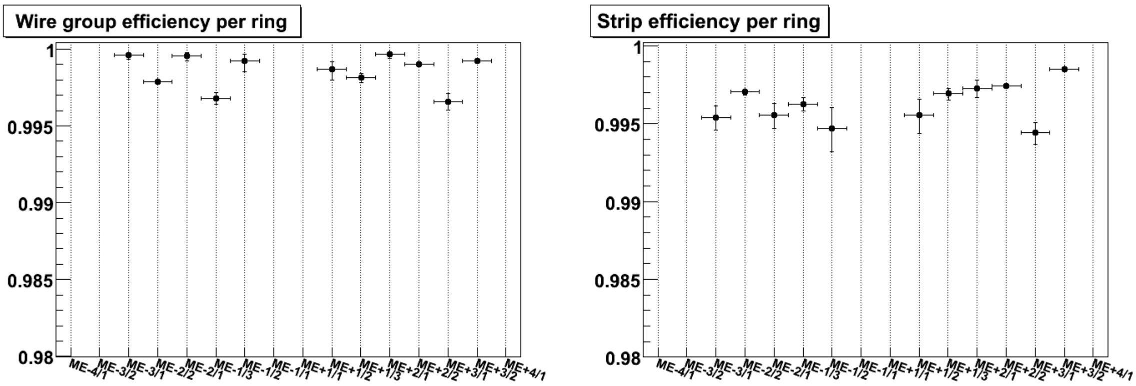

Figure 11: A summary of wire group (left) and strip (right) digi efficiencies, over all functioning chambers in a ring. Some rings are inaccessible in this study with CRAFT data.

The average wire group and strip digi efficiencies are shown in Fig. 11. Typically, all six layers are highly efficient, greater than 99.4%.

6.1.3 Rechit Efficiency

The efficiency for reconstructing a rechit is measured for each layer in a chamber. The chamber is efficient if the rechits are found in a given layer - there is no requirement on the distance between the rechit and the interpolated point. Also, no quality requirements are placed on the individual rechits as part of the measurement of rechit efficiency.

The rechit efficiency will be a convolution of the strip and wire group digi efficiencies. It might also depend on some of the details of the rechit reconstruction algorithm, especially as regards quality or other criteria applied to the strip and wire signals. The rechit efficiency for all the CSC rings is shown in Fig. 12. The rechit reconstruction efficiency is above 99.3%.

6.1.4 Segment Efficiency

It should be possible to build a segment if at least three good rechits are recorded along the muon trajectory. The chamber is efficient if a segment has been reconstructed. No matching criteria have been applied (cf. Fig. 9).

Ideally, the segment efficiency would be related in a simple and direct way to the rechit efficiency. The segment reconstruction algorithm, however, also places requirements on the rechits used to build segments. It does not find segments in chambers with very many hits, due to prohibitive combinatorial problems – this will register as an inefficiency in the present study. The segment efficiency for all the rings in the CSC system is shown in Fig.12. For cosmic rays, the overall segment efficiency is above 99%.

6.1.5 Attachment Efficiency

The attachment efficiency is a characteristic of the segment finder. It is defined as the probability of the segment to use a rechit from a given layer if there are rechits in that layer. The segment finder could reject some rechits if their quality were poor, or if they were producing a bad fit, so one can anticipate a small inefficiency with respect to the efficiency for producing rechits. What is important is that this inefficiency should be the same for all layers. Any significant variation with layer number would be a hint of a problem – for example, an unacceptable dependence on the track angle. Fig. 13 shows that there is no bias in the CRAFT data.

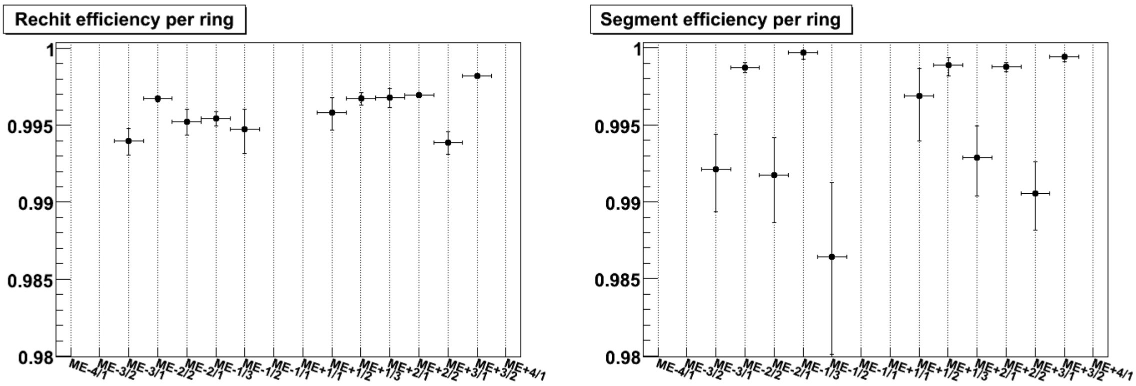

Figure 12: Summaries of rechit and segment efficiencies, analogous to Fig. 11

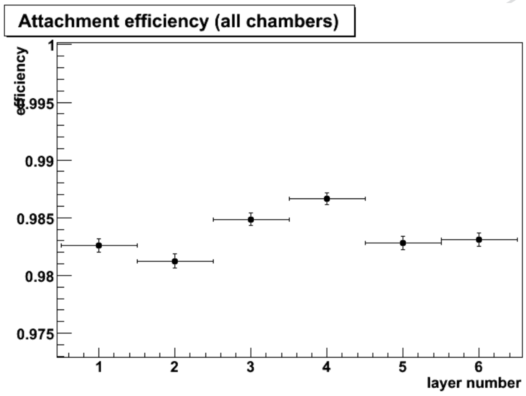

Figure 13: The attachment efficiency for each layer

Table 1: A summary of efficiencies for chambers in good operating condition

quantity	typical efficiency (%)
ALCT	> 99.9
CLCT	> 99.9
wire digis	> 99.5
strip digi	> 99.4
rechit	> 99.3
segment	> 98.5

Given the excellent efficiencies measured at all levels of the readout and reconstruction, an estimate of the efficiency for reconstructing muons in collision data would be plausible. A sample of simulated $W \rightarrow \mu\nu$ decays was used to make such an estimate: for all chamber types, the efficiency to reconstruct a segment is above 99%, if the muon passes through the chamber – regardless of whether the muon goes through a good region or close to a high voltage boundary or the periphery of the chamber. According to the same simulation, the efficiency to reconstruct a stand-alone muon is above 95% in the η range covered by the CSCs.

In summary, all the basic efficiencies have been shown to be high, for chambers in good operating condition during CRAFT. See Table 1.

7 Resolution

The CRAFT data were used to study and measure the spatial resolution of the CSCs as they are meant to be operated for early physics [2]. The purpose of this study is to demonstrate that all working chambers perform as they should, before colliding beams commence. Excellent earlier studies of CSC spatial resolution can be found in Ref. [19, 20].

The following sections define what we mean by "resolution," and how we measure it. We show the expected variations of the resolution as functions of charge, position within a strip, the width of the strip, and angle. Special studies have been carried out for ME$\pm$1/1 chambers, as their design differs somewhat in order to cope with the high magnetic field and difficult demands for resolution [17]. We report measured values of the resolution for all types of chambers, and then conclude.

7.1 Analysis

The reconstruction of muon trajectories and the measurement of the muon momentum depends critically on the spatial resolution of the chambers. The most important coordinate is ϕ, so these studies are concerned with the strip measurements only. An adequate measurement of R at a given z is given by the anode wires.

7.1.1 Methodology

The *resolution* is the typical measurement error. It is determined by the design parameters of the chamber (width of the cathode strip, distance to the anode wire plane, high voltage, anode wire radius and pitch, gas mixture, electronics noise and cross talk) as well as certain characteristics of each muon track (angle, position with respect to the center of the struck strip, and amount of charge collected), and of course the physics of multi-wire proportional chambers (electron diffusion, magnetic field influence) and the reconstruction (reduction of data and knowledge of misalignments). The distribution of hit residuals with respect to the muon trajectory can give a good measure of the resolution. A *residual* is the difference between the measured coordinate and the true or estimated true (i.e., predicted) coordinate.

For the purposes of the study, the coordinate of interest is the coordinate measured by the strips. In global coordinates, this would be $R\phi$ as measured in centimeters, but most of the results presented here are couched in *strip coordinates*. The strip coordinate, s, is the $R\phi$ coordinate relative to the center of the strip, divided by the strip width at the position of the hit. Modulo resolution effects, one has $-0.5 \leq s \leq 0.5$. Most of the plots here will show residuals

[2] The current high voltage settings are intentionally lower than what was used for the test beam studies, in order to avoid aging the chambers unnecessarily during commissioning periods. This has a significant impact on the spatial resolution, as described below

Table 2: Selected relevant physical specifications of the cathode strip chambers. For more information, see Ref. [1]

ring	chambers per ring	strips per chamber	strip width (mm)	(mrad)
ME±1/1*a*	36	48	4.11 – 5.82	3.88
ME±1/1*b*	36	64	4.44 – 7.6	2.96
ME±1/2	36	80	6.6 – 10.4	2.33
ME±1/3	36	64	11.1 – 14.9	2.16
ME±2/1	18	80	6.8 – 15.6	4.65
ME±2/2	36	80	8.5 – 16.0	2.33
ME±3/1	18	80	7.8 – 15.6	4.65
ME±3/2	36	80	8.5 – 16.0	2.33
ME±4/1	18	80	8.6 – 15.6	4.65

distributions in strip coordinates. In order to obtain a resolution in physical units, we multiply by the mean width of a strip in the given chamber. A synopsis of relevant chamber parameters is given in Table 2.

The residuals distribution is not Gaussian, in general, so one must settle on a measure of the residuals distribution to be identified with the “resolution” of the given chamber. Usually we fit the distribution with a sum of two Gaussian functions, with zero mean, using the functional form:

$$f(x) \equiv \frac{A_1}{\sqrt{2\pi}\sigma_1} \exp\left(\frac{-x^2}{2\sigma_1^2}\right) + \frac{A_2}{\sqrt{2\pi}\sigma_2} \exp\left(\frac{-x^2}{2\sigma_2^2}\right) \tag{4}$$

where optimal values for the parameters σ_1, σ_2, A_1 and A_2 are obtained from the fit. We take the resolution to be:

$$\text{resolution :} \qquad \bar{\sigma} = \sqrt{\frac{A_1\sigma_1^2 + A_2\sigma_2^2}{A_1 + A_2}}. \tag{5}$$

If one Gaussian suffices, then we take simply the σ parameter of the single Gaussian. We do not take the r.m.s. as the residual distributions often have long non-Gaussian tails which inflate the r.m.s. - these tails are caused by δ-ray electrons and fall outside a discussion of the core resolution. The residuals distributions of the eight chamber types with fits to Eq. 4 are given in Fig. 14.

As defined, the resolution $\bar{\sigma}$ pertains to a hit in a *single layer*. The resolution of a chamber is more complicated, since it depends on the number of hits in the segment, the angle of the segment, the generally non-normal angle between wire groups and strips, and the fact that the strips are staggered layer-by-layer for all chambers except ME±1/1. We can take the special case of segments with six hits that are normal to the chamber and pass through the center. If the residuals distribution near the edge of a strip has Gaussian width σ_e, and near the center of a strip, σ_c, then to a good approximation, the resolution for the segment is

$$\text{segment :} \qquad \sigma_{\text{seg}} = \left(\frac{3}{\sigma_e^2} + \frac{3}{\sigma_c^2}\right)^{-1/2}. \tag{6}$$

We will use this expression to characterize the chamber resolution.

Another method for measuring the resolution does not rely on the residuals of a single layer, but rather on the value of χ^2 for the linear fit to all six hits. Let us define the *unweighted* χ^2 as

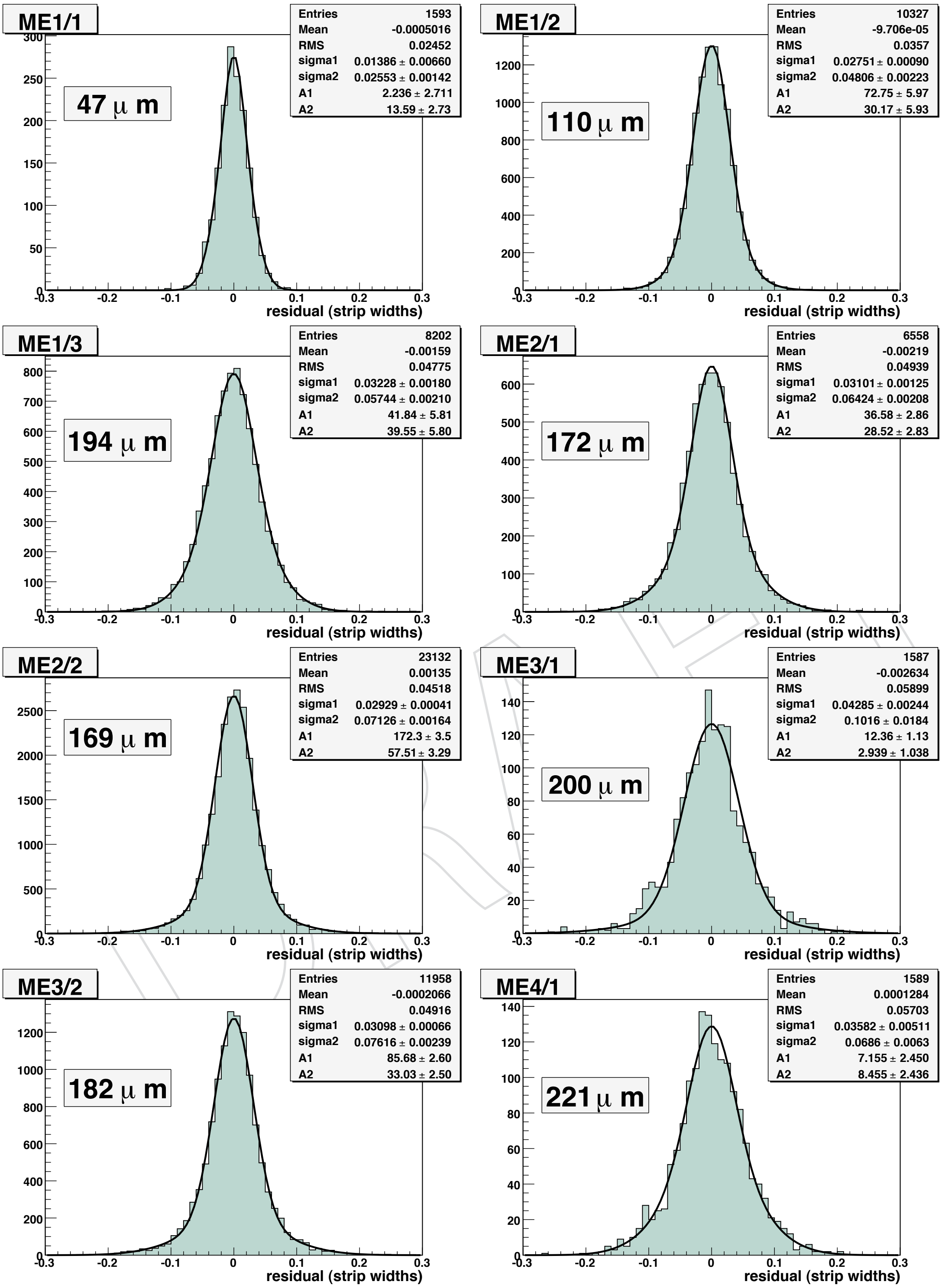

Figure 14: Distributions of residuals fit to the double-Gaussian function given in Eq. 4.

follows:

$$\chi_0^2 \equiv \sum_{i=1}^{6} (s_i - (a + bi))^2 \tag{7}$$

where a and b are free parameters, and the layer number i plays the role of the z coordinate. Notice we have set all uncertainties to one. As a consequence, $\langle \chi_0^2 \rangle = 4\sigma_0^2$, where σ_0 is the effective uncertainty on s_i.

We do not have a good exterior measure of the position of the muon, so we have to use the segment itself. Perhaps the cleanest procedure is to use five out of the six hits on a good segment to predict the position of the sixth. In practice, we fit the hits in layers 1, 2, 4, 5 and 6 to a straight line to predict the "correct" position in layer 3, and then compare to the measured position in layer 3. Monte Carlo studies show that the width of the residuals distribution is inflated by about 10% due to the measurement error from the five-hit fit; this uncertainty is larger for layers 1, 2, 5 or 6. We do not remove this 10% inflation for the results reported in this note.

7.1.2 Expected Behavior

The resolution is known to vary with several quantities, including the charge recorded for that hit, the position within the strip, the physical width of the strip, the inclination of the track and the magnetic field, among others. This behavior can be understood qualitatively, given a model for the formation of signals on the strips.

Analytical calculations for the formation of signals in cathode strip chambers have been available for many years. Gatti described how charge was apportioned among the strips in 1979 [21]. His calculation was updated and extended by Mathieson and Gordon in 1984 [22].

A simple picture of the signal on three strips labels the charges Q_L, Q_C and Q_R, where by definition the charge on the central strip is larger than that on the left and right side strips. The central strip extends across $-0.5 < s < 0.5$, and the left strip is at $s = -1$ and the right, at $s = +1$. With the muon passing through the central strip slightly to the right of the center of the center strip ($s > 0$), $Q_R > Q_L$, and of course $Q_C > Q_R$.

It is intuitively clear that the position of the muon relates to the relative difference $Q_R - Q_L$, and indeed the first approximation to this position is simply

$$s \approx \frac{1}{2} \frac{Q_R - Q_L}{Q_C - \min(Q_R, Q_L)}. \tag{8}$$

For a justification of this choice, see Ref. [19]. Other choices can be made - this is not critical for the present discussion.

The accuracy of the measurement of s depends on how well the difference $Q_R - Q_L$ can be measured. For the CSCs, most of the charge appears on the central strip, unless the muon passes quite close to the edge of the strip. For the large chambers especially, Q_R and Q_L are only a few percent of Q_C, and in the worse cases are not much larger than the pedestal width. This width characterizes the electronics noise, so the central question is: are the observed charges Q_R and Q_L larger than or comparable to this noise?

If the total charge Q is large, then the impact of the noise will be reduced. This explains why the resolution improves as Q increases, so long as δ-ray electrons are not interfering with the charge distribution. Explicit calculations show that the resolution should be proportional to $1/Q$ [21, 22].

The charge on the right strip will increase as the muon trajectory approaches $s = 0.5$. In the limit that $s \to 0.5$, Q_L does not matter, and the approximation in Eq. 8 becomes

$$s \approx \frac{1}{2}\frac{Q_R}{Q_C} \to \frac{1}{2}$$

since $Q_R \to Q_C$ in this limit. In such a case, the electronics noise becomes relatively unimportant, since both Q_R and Q_C are substantial. In contradistinction, as the muon trajectory approaches $s = 0$, both Q_L and Q_R are minimal and therefore maximally impacted by electronics noise, making the difference $Q_R - Q_L$ relatively difficult to measure. For these reasons, one expects the best resolution for muon trajectories close to the edge of the strip, and the worst resolution when they go through the center.

The spatial distribution of the charge depends on the separation between strips, for a fixed distance between the strip plane and the anode wire plane. If the physical width of the strip is large, then Q_L and Q_R will be small. Due to the impact of electronics noise, which tends to be larger when the strips are larger, the resolution is poorer in chambers with large strips than in chambers with small strips. For this reason, the strips in the ME$\pm1/1$ chambers have been made particularly small (cf. Table 2), since they play a key role in the momentum measurement in the end caps [1].

Finally, a muon which passes through the anode plane at an oblique angle (with respect to the strips) will produce a relatively broad distribution of charge across the gas gap, leading to a smearing of the distribution of charges Q_L to Q_R, and a poorer resolution.

The above discussion is heuristic in nature; the actual calculation of coordinates and uncertainties is based on the full Gatti function and on quantitative studies of the variation of resolution with charge, position within a strip, and strip width. For a detailed technical discussion of precise position measurement with cathode strip chambers, see, for example, Ref. [23].

7.1.3 Qualitative Results from CRAFT

Events were selected which contained a good segment from which residuals distributions for layer 3 could be formed. A good segment was one which contained six rechits and $\chi^2 < 200$ (unreduced). An event was selected if it contained at least one good segment. In order to retain only clean events, any event with more than eight segments of any quality were rejected, as well as events with more than fifty rechits. The event was also rejected if any chamber contained more than four segments of any quality. About 5×10^4 events were selected [6].

Further criteria were applied when filling residuals distributions, to ensure that the results were based on the cleanest possible segments and hits:

1. the estimated errors on the six rechits have to be smaller than 0.2 strip widths. This eliminates rechits based on a single strip or for which the cross-talk correction led to negative values for Q_R and Q_L.

2. The sum of charges for three strips and three time slices for layer 3 could not be too small or too large: $250 < Q_{3\times3} < 1000$ ADC counts.

3. The segment inclination should correspond to tracks originating roughly from the interaction point:

$$-1 < \frac{dy}{dz} < -0.15 \qquad \text{and} \qquad \left|\frac{dx}{dz}\right| < 0.15 \tag{9}$$

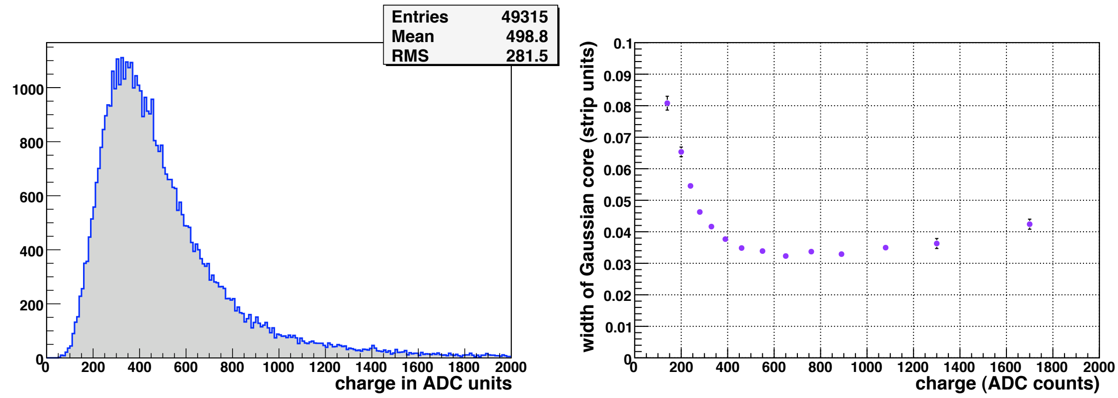

Figure 15: *Left:* Observed charge distribution, $Q_{3\times3}$, in ADC counts. *Right:* Variation of the *per layer* resolution as a function of $Q_{3\times3}$. This measurement was made using chambers in ME±2/2 and ME±3/2; other chambers give very similar results.

where these are local coordinates: dy/dz is the angle with respect to the anode wires, and dx/dz is the angle with respect to the cathode strips.

4. The strip coordinates were fit to a straight line. The resulting χ^2 value were required to be less than 9 for the 5-hit fit, and less than 50 for the 6-hit fit.

These cuts were relaxed singly when checking the impact of these criteria.

In the remainder of this section, we use the CRAFT data to demonstrate the expected behavior as described in Section 7.1.2. No attempt was made to remove layer-by-layer misalignments, as these are known to be small compared to the resolution.

The "charge" depends on several factors, including the gas composition, pressure, high voltage, amplifier gain, and of course the ionization of the gas by the muon. We denote by $Q_{3\times3}$ the sum of the charges recorded in three time bins across three consecutive strips [19]. A distribution of $Q_{3\times3}$ for the CRAFT data is shown in Fig. 15 (left). The distribution has a long tail, similar to that expected from the Landau distribution.

A summary of the variation of the resolution as a function of charge is given in Fig. 15 (right). Chambers in rings ME±2/2 and ME±3/2 were selected for this plot, since they have the largest number of events in CRAFT. The cuts on the χ^2 of the 2-dimensional strip fit were relaxed for this study, so that the impact of δ-ray electrons is evident at large angles. If the cuts are imposed, then the rise for $Q_{3\times3} > 800$ ADC counts is eliminated.

Another demonstration of the sensitivity of the resolution to charge is provided by two runs taken outside of the CRAFT exercise, in which the high voltage was raised by 50 V. Since the number of events was modest, the event and segment selection was somewhat looser than described above. The improvement in resolution is consistent with the expected $1/Q$ behavior, as demonstrated in Fig. 16.

The variation of the resolution with the position withing a strip, s, is shown in Fig. 17. For the ME±2/2 chambers, the resolution in the center of the strip is worse by about a factor of two than at the edge. This variation is weaker for chambers with thinner strips, such as ME±1/2 and ME±1/1.

Most of the analysis presented here is done in terms of the normalized strip width, s. The physical width of the strip matters, too. For broad strips, most of the charge is collected on the

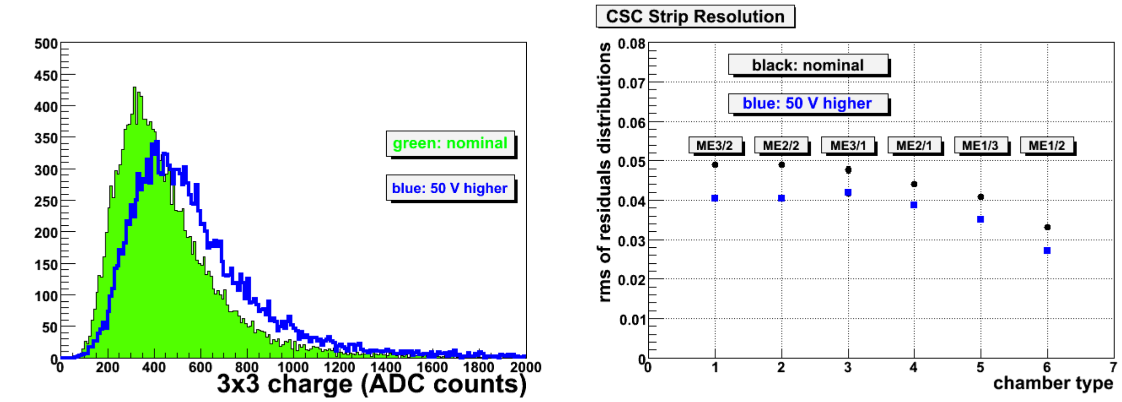

Figure 16: *Left:* Charge distributions for two consecutive runs. The solid histogram corresponds to the nominal setting, and the open histogram corresponds to an increase of 50 V. *Right:* Comparison of the resolution for the same two runs.

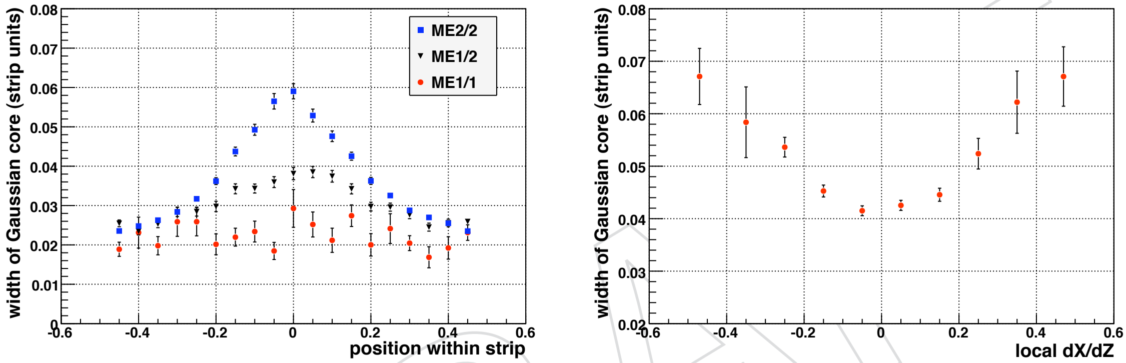

Figure 17: *Left:* Variation of the *per layer* resolution as a function of s, the position within the strip, for three different types of chambers. *Right:* Variation as a function of local dx/dz, which quantifies the segment inclination with respect to the strips. These measurements were done with the ME±2/2 chambers.

central strip, leaving a small amount for Q_L and Q_R, leading to a poorer resolution. For this reason, the smaller chambers have a much better resolution than the larger chambers. Within a chamber, there is a mild variation of the resolution along the strip, since the strip is narrower at the narrow end of the chamber and wider at the broad end.

The results described above were derived for muon trajectories that were nearly perpendicular to the strips. For low-momentum muons coming from the interaction point, however, more oblique trajectories are possible. We have observed a clear variation of the resolution as a function of dx/dz in chambers from ring ME±2/2, see Fig. 17. For all other results reported in this note, a tight cut on $|dx/dz|$ has been applied (Eq. 9).

The estimated uncertainty is computed taking into account variations as a function of charge, position within a strip, and strip width. Distributions of normalized residuals ("pull distributions") allow us to check those calculations. A summary of the pulls for all chamber types is given in Table 3. Overall, the pulls are somewhat too wide, especially for the ME±1/1 chambers, indicating that the uncertainties are slightly underestimated. It will be possible to adjust the error estimates on the basis of the CRAFT data.

Table 3: Resolution *per layer* for each chamber type, and the rms of the pull distributions

ring	resolution				pull r.m.s.
	fit to two Gaussians		*derived from* χ_0^2		
	strip widths	μm	strip widths	μm	
ME±1/1	0.024 ± 0.002	128	0.021	115	1.89 ± 0.06
ME±1/2	0.034 ± 0.001	285	0.036	300	1.34 ± 0.01
ME±1/3	0.044 ± 0.001	578	0.050	658	1.52 ± 0.01
ME±2/1	0.046 ± 0.001	510	0.054	600	1.28 ± 0.02
ME±2/2	0.040 ± 0.001	487	0.048	581	1.42 ± 0.01
ME±3/1	0.054 ± 0.002	633	0.064	751	1.26 ± 0.04
ME±3/2	0.044 ± 0.001	534	0.050	614	1.37 ± 0.02
ME±4/1	0.054 ± 0.004	648	0.064	766	1.17 ± 0.03

7.1.4 Measurements of the Nominal Resolution

The results in the previous section demonstrate the expected qualitative behavior of the resolution. In this section, we quantify the resolution of the CSCs, as measured with CRAFT data, in order to verify that they are performing as designed.

Residuals distributions for chambers in each ring were fit to the sum of two Gaussian functions (Eq. 4), and the resolution computed according to Eq. 5. These distributions are shown in Fig. 14. Table 3 lists the *per layer* resolution obtained in this manner. The values given in μm are obtained by multiplying the resolution in strip widths by the average width of the strip (see Table 2).

We formed distributions of χ_0^2 (Eq. 7) for each chamber type. We computed σ_0 (which would be in units of the strip width) and converted to an uncertainty in μm using the average physical strip width. The results are listed in Table 3. These values agree very well with the values obtained from the fit to two Gaussian functions.

The resolution of a chamber, given six good rechits, can be estimated on the basis of the *per layer* resolution. One can simply take the numbers listed in Table 3 and divide by $\sqrt{6}$, or one can perform a slightly more refined analysis indicated by Eq. 6. The latter gives systematically lower values for the resolution than the former. Table 4 lists both sets of values, which can be compared to the design values [1]. Most the observed values are somewhat higher, except for the ME±1/1 chambers, which are significantly better than design. The fact that the high voltage is set to a somewhat reduced value is the primary reason for the slightly worse resolution in the non-ME±1/1 chambers.

7.1.5 Special Studies of ME1/1

The ME±1/1 chambers play a special role. First, they prove the key measurements for the high-momentum muon tracks expected at high $|\eta|$. And second, they must operate in a very high magnetic field, which alters the drift of the electrons inside the gas layers. For these reasons, the gas gaps are smaller, the gas gain is higher, the strips are narrower, and the wires are tilted with respect to wires in the other chambers [17].

The drift of the electrons perpendicular to the anode wires depends sensitively on the magnetic field. Most of the CRAFT data were taken at full field, but some data were taken with zero field, and with some intermediate values. These data were analyzed to measure the resolution as a function of the magnetic field, with the results shown in Fig. 18 (left). Clearly the resolution is

Table 4: Resolution *per chamber* for each chamber type

ring	resolution (μm)		
	design	*per layer* / $\sqrt{6}$	Eq. 6
ME±1/1	75	52	47
ME±1/2	75	116	110
ME±1/3	150	234	194
ME±2/1	150	208	172
ME±2/2	150	199	169
ME±3/1	150	258	200
ME±3/2	150	218	182
ME±4/1	150	264	221

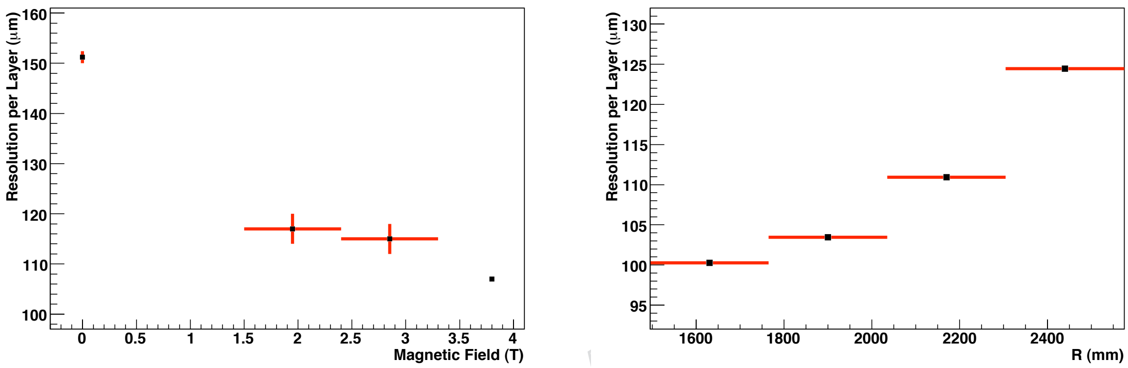

Figure 18: *LEFT:* Variation of the resolution in the ME±1/1b chambers as a function of magnetic field in Tesla. *RIGHT:* Variation of the resolution as a function of the radius (distance from the beam line)

best at full field, confirming the details of the initial design.

The radial extent of the ME±1/1b chambers was divided into four regions in order to check the resolution at different radii. Fig. 18 (right) shows that the resolution is best near the beam line, where it is most critical, and rises rapidly with radius. A further study of the resolution for different azimuthal regions of the ME±1/1b chambers shows a mild variation with the angle of the anode wires, confirming the choices made in the design of these chambers.

8 Timing

The readout of the cathode strips provides enough information to reconstruct the pulse shape and infer the time of the signal. The output from the cathode strip front-end amplifier is sampled every 50 ns (2 BX) with the results stored in a switched capacitor array (SCA). The arrival of the pulse is arranged so that the first two time bins are free from signal, allowing a dynamical estimate of the signal base line. A good description of the pulse shape recorded in the SCA is given by a 5-pole semi-Gaussian:

$$S(t) \propto \left(\frac{t - T_S}{T_0}\right)^4 \exp\left(-\frac{(t - T_S)}{T_0}\right)$$

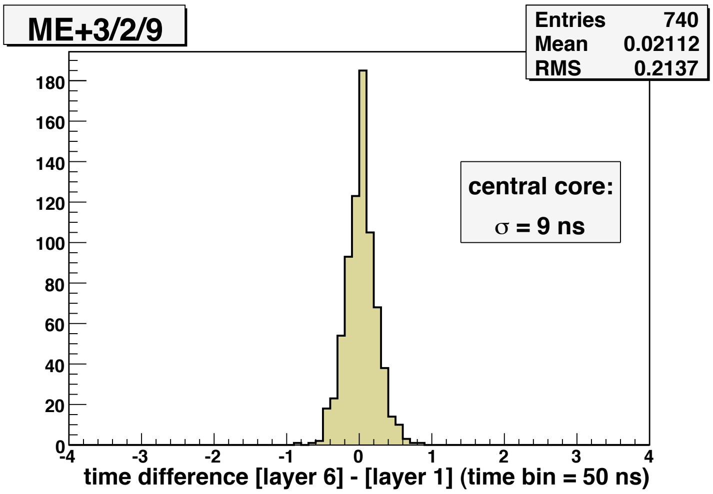

Figure 19: The difference in rechit times for layers 6 and 1 in chamber $ME + 2/2/9$. Units are 50 ns time bins. A fit of the central core to a Gaussian function gives a width of 9 ns.

valid for $t > T_S$, the start time. Given the fixed exponent of the $(t - T_S)$ term, the shape of the pulse is determined by the decay constant T_0. The maximum occurs at $t = T_S + 4T_0$.

This pulse shape is very well established through studies with prototypes [20] as well as with cosmic ray data. Cross-talk is approximately 10% of the signal, and should be taken into account in order to describe the pulse shape precisely.

We used the CRAFT data to make some simple tests of the timing capabilities of the CSCs. The time of flight of a muon through a single chamber is quite small, essentially zero compared to the 25 ns BX spacing. Fig. 19 shows the distribution of differences in measured times for layers 6 and 1, in units of 50 ns time bins. The mean is consistent with zero, and the r.m.s. is 0.143 bins, which corresponds to 7.2 ns, or 5 ns per layer. Most segments have six rechits (cf. Fig. 4), so a single segment should have a time resolution of about 2 ns. This compares well with the transit time of a muon from the interaction point to the CSCs of roughly 30 ns, and of the beam crossing time of 25 ns.

Improvements to the use of the strip timing information can be foreseen, based on a more detailed analysis of the subtle effects of cross talk and noise correlations, as suggested by pilot studies with test beam data [20].

It is hoped to use this timing capability for rejecting out-of-time hits and tagging the time of the muon independently of the trigger system.

9 Summary

An assessment of the performance of the CSCs has been completed using the large CRAFT data sample recorded in Fall 2008. More than 97% of the CSC muon detector system was in excellent working condition and participated in the bulk of this campaign. The agreement of basic global quantities between the real data and simulation is good. The fraction of channels which provided no signal, or were noisy, is very small, less than 1%. All of the essential efficiencies have been measured, ranging from the local charged tracks which trigger the chamber readout through the reconstruction of segments. These efficiencies are all very high. The position resolution has been studied, with variations observed as a function of several relevant variables, such as the charge, position within a strip, high voltage, track inclination, and in the case of the ME±1/1 chambers, of the magnetic field, radius and wire tilt. The measured chamber resolutions are not quite as good as design, due to an intentional reduction of the high voltage, except for the ME±1/1 chambers, which surpass the design criterion. Finally, the potential timing capabilities of the CSCs was briefly investigated.

The prospects for future studies are very good. The operating conditions of the CSC subsystem have been improved since the CRAFT data were taken, and one can anticipate that the CSC subsystem will function extremely well once the LHC delivers collisions to CMS.

References

[1] CMS Collaboration, *CMS – The Muon Project*, CERN/LHCC 97-32

[2] CMS Collaboration, *"CMS Physics Technical Design Report"*, CERN/LHCC 2006-001 (2006)

[3] J. Hauser et al., *"Experience with Trigger Electronics for the CSC System of CMS"*, Proceedings of the 10th Workshop on Electronics for LHC Experiments and Future Experiments (2004)

[4] N. Terentiev, T. Ferguson and M. Ignatenko, *Performance of the CMS Endcap Muon Anode-Wire Front-end Electronics in the CRAFT 2008 Data*, CMS-NOTE, submitted

[5] S. Stoynev and M. Schmitt, *Efficiency Measurements in the CSC Muon Endcap System*, CMS-NOTE, in preparation

[6] I. Bloch et al., *Measurement of the CSC Spatial Resolution with Cosmic Ray Muons*, CMS-NOTE, in preparation

[7] V. Perelygin et al., *ME1/1 CSC Spatial Resolution*, CMS NOTE, submitted.

[8] R. Breedon et al., *Post-Production Testing and Commissioning of the CMS End-cap Cathode Strip Chambers*, CMS-NOTE, in preparation

[9] CMS Collaboration, *Studies of CMS Muon Reconstruction Performance with Cosmic Rays*, in preparation

G. Abbiendi et al., *Muon Reconstruction in the CMS Detector*, CMS-AN/2008-097

[10] CMS Collaboration, ALIGNMENT PAPERS

[11] CMS Collaboration, MAGNETIC FIELD MAP PAPER

[12] P. Biallass, T. Hebbeker, K. Hoepfner, *Simulation of Cosmic Muons and Comparison with Data from the Cosmic Challenge using Drift Tube Chambers*, CMS NOTE-2007/024 (2007)

[13] W.-M. Yao et al., Journal of Physics **G33** 1 (2006)

[14] D. Acosta et al., *Large CMS Cathode Strip Chambers: Design and Performance*, Nucl. Instrum. Meth. **A453**, 182-187 (2000).

[15] CMS Collaboration, *The CMS Experiment at the CERN LHC*, Journal of Instrumentation (JINST) **3**, S08004 (2008).

[16] T. Ferguson, N. Terentiev, I. Vorobiev, N. Bondar, A. Golyash, and V. Sedov, *Anode Front-End Electronics for the Cathode Strip Chambers of the CMS Endcap Muon Detector*, Nucl. Instrum. Methods Phys. Res. **A539**, 386-406 (2005) [CMS-Note 2004/003]

[17] Yu V. Erchov et al., *Cathode Strip Chamber for CMS ME1/1 Endcap Muon Station*, Physics of Paticles and Nuclei Letters, Vol. 3, No. 3, (2006) 183.

[18] D. Acosta et al., *Measuring Muon Reconstruction Efficiency from Data*, CMS NOTE-2006/060 (2006)

D. Acosta et al., *Efficiency of Finding Muon Track Trigger Primitives in CMS Cathode Strip Chambers*, Nucl. Instrum. Meth. **A592** (2008) 26 [CMS Note 2007/031]

[19] V. Barashko et al., *Fast Algorithm for Track Segment and Hit Reconstruction in the CMS Cathode Strip Chambers*, Nucl. Instr. Meth. **A589/3** (2008) 26 [CMS NOTE 2007/023]

[20] TESTBEAM STUDIES. *Please help specify these.*

[21] E. Gatti et al., *Optimum Geometry for Strip Cathodes or Grids in MWPC for Avalanche Localization Along the Anode Wires*, Nucl. Instrum. Meth. **163** (1979) 83

[22] E. Mathieson and J. Gordon, *Cathode Charge Distributions in Multiwire Chambers: I. Measurement and Theory*, Nucl. Instrum. Meth. **227** (1984) 267; *op. cit., II. Approximate and Empirical Formulae*, Nucl. Instrum. Meth. **227** (1984) 277

[23] I. Golutvin et al., *Cathode Strip Chambers Data Analysis*, Proceedings of the Seventh International Conference on Advanced Technology and Particle Physics, Como, Italy, 15-19 October 2001